Progress In Electromagnetics Research M, Vol. 64, 43–54, 2018

3-D V2V MIMO Channel Modeling in Different Roadway Scenarios with Moving Scatterers

Derong Du[1], Xiaoping Zeng[1, *], Xin Jian[1], Fan Yang[1, 2], and Meng Sun[1]

Abstract—Vehicle-to-Vehicle (V2V) communications are characterized by dynamic environments due to the movement of the transceiver and scatterers. This characteristic makes V2V channel modeling particularly challenging. In this paper, a three-dimensional (3-D) geometrical propagation model and a generalized 3-D reference model that include line-of-sight (LoS) and single bounced (SB) rays are proposed for multiple-input-multiple-output (MIMO) V2V multipath fading in different roadway scenarios (e.g., flat roads, intersections and arcuate overpasses). In the models, the transceiver can move with nonlinearly varying velocities in nonlinearly varying directions, and each scatterer can move with a random velocity in a random direction. The corresponding space-time correlation functions (ST-CFs) are analytically investigated and numerically simulated in different roadway scenarios. Finally, the modeled Doppler power spectral density (D-PSD) is compared with the available measured data. The close agreements between the modeled and measured D-PSD curves confirm the utility of the proposed model.

1. INTRODUCTION

The vehicle-to-Vehicle (V2V) communication has received much attention in recent years due to its significant societal benefit and commercial value to delivering safety, mobility and convenience applications for the automobile transportation. Different from the conventional fixed-to-mobile (F2M) cellular systems, V2V communications allow both the transmitter and receiver to be in motion. Suitable channel models and channel characterizations are absolutely essential for successful design of V2V systems. However, V2V communications are characterized by a dynamic environment with the moving transceiver and scatterers that make V2V propagation and channel modeling particularly challenging.

Many V2V channel models have been proposed in various ways, and they can be traced back from fixed scattering models to moving scattering models. Many V2V channel models with the assumption of stationary scatterers have been proposed such as the fixed scattering models in [1] and [2]. However, the moving scatterers are unavoidable in V2V communications, and moving foliage, walking pedestrians and passing vehicles [3] are only a few examples of scatterers in motion. A non-stationary multiple-input-multiple-output (MIMO) V2V channel model was derived from the geometrical street model, and the impact of fixed and moving scatterers on the statistics of MIMO V2V channel was studied in [4] and [5]. A single-input-single-output (SISO) V2V channel model was proposed in which the local scatterers can move with random velocities in random directions, and the corresponding autocorrelation function, power spectral density, and the Doppler spread of the channel were derived, shown, and confirmed by the available measurement data for different scatterer velocity distributions in [6] and [7]. Modeling of mobile scatterer clusters for Doppler spectrum in wideband V2V communication channels in an urban canyon environment was investigated in [8] and [9]. A three-dimensional (3-D) fixed scattering and

Received 19 October 2017, Accepted 12 January 2018, Scheduled 19 January 2018
* Corresponding author: Xiaoping Zeng (zxp@cqu.edu.cn, dr_du@cqu.edu.cn).
[1] College of Communication Engineering, Chongqing University, Chongqing 400044, China. [2] Chongqing Jinmei Communication Co. Ltd, Chongqing 400030, China.

two-dimensional (2-D) moving scattering narrowband reference channel model that includes stationary and moving scatterers was proposed in [10], and this work was extended to wideband channels in [11]. The two-cylinder models in [10] and [11] imposed some constraints on the position of the local scatterers and assumed the velocities of scatterers were constant. A dynamic geometry-based scattering model for street wideband MIMO V2V fading channel was proposed in [12], and it is assumed that the static and mobile scatterers were uniformly distributed on time-varying ellipses and time-varying segment of the road, respectively. A geometry-based stochastic scattering model (GBSSM) for wideband MIMO V2V channels was proposed in [13], and the proposed GBSSM with cross-polarized antennas combined 3-D two-cylinders to model the stationary scatterers and 2-D multi-rings to imitate the moving scatterers.

All previously reported models in [4–13] are 2-D moving scattering models. However, in urban measurements typically 90% of the received power is contained in paths with elevations up to 40° [14]. Another measurement campaign in different environments [15] reports mean elevations of the received power from 1.8 for outdoor-indoor environments, up to 17.1° for urban macrocell environments. Therefore, the 2-D scattering assumption does not seem to be appropriate for many communication scenarios, for example, urban V2V communications in which the transmitter and receiver antenna arrays are often located in close proximity to or lower than the surrounding scatterers. Moreover, many vehicles as well as scatterers have different altitudes in mountain cities (e.g., Chongqing in China). Those observations give a motivation for a more general 3-D model of the V2V multipath channel. The 3-D isotropic moving scattering was considered,and a generic statistical characterization of the V2V SISO channel was presented by adopting a stochastic modeling approach in [16]. A 3-D generic MIMO V2V fading channel model that includes line-of-sight (LoS), single bounced (SB), and multiple bounced (MB) rays was proposed in [17]. All previously reported 2-D and 3-D moving scattering models have assumed that the transceiver moves with a constant velocity in a constant direction. However, vehicles generally move with varying velocities in varying directions in the actual V2V communications, especially in some roadway scenarios (e.g., intersections and arcuate overpasses). In [18], a 2-D fixed scattering mobile-to-mobile (M2M) SISO channel model was analyzed, where the transmitter and the receiver could experience changes linearly in their velocities. However, the assumption that the transceiver experiences changes linearly in velocities is only appropriate for certain communication scenarios, for example, V2V communications on the uncrowded highway. For the actual urban V2V communications, the velocity and direction of the vehicles change nonlinearly due to the traffic congestion, turning, up and down in different roadway scenarios.

According to the above review, the model and statistical properties of 3-D V2V MIMO moving scattering channels taking account of velocity and direction variations of the transceiver have been rarely investigated so far. This paper strives to alleviate the current lack by investigating the model and statistical properties of a narrowband 3-D V2V MIMO channel in different roadway scenarios (e.g., flat roads, intersections and arcuate overpasses) in which the local scatterers can move with random velocities in random directions, and the transceiver can move with nonlinearly varying velocities in nonlinearly varying directions. The proposed reference model constructs the channel impulse response as a combination of LoS and SB components. From the reference model, the corresponding space-time correlation functions (ST-CFs) are analytically investigated and numerically simulated indifferent roadway scenarios. Finally, the modeled Doppler power spectral density (D-PSD) results with measured data in [19] are compared. The close agreements between the analytically and empirically obtained D-PSDs confirm the utility of the proposed model and show the importance of including moving scatterers, nonlinearly varying velocities and directions of the transceiver motion in propagation models.

2. GEOMETRICAL MODEL AND REFERENCE MODEL FOR 3-D MIMO V2V CHANNELS

2.1. Geometrical Model

The V2V communication is shown in Fig. 1. The radio propagation environment is characterized by the 3-D movement of scatterers and the transceiver. Both transmitter T_X and receiver R_X are equipped with uniform linear arrays consisting of omnidirectional antenna elements. It is assumed that the SB waves emitted from the qth antenna element of T_X at an angle of departure (AoD) reach the pth antenna element of R_X at an angle of arrival (AoA) after being scattered by the local moving scatterers. The

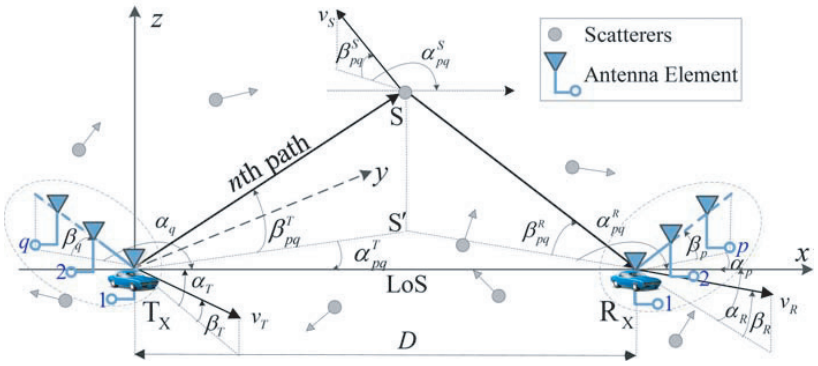

Figure 1. Geometrical model with LoS and SB rays for the 3-D MIMO V2V communication scenario.

geometrical model does not impose specific constraints on the position of the local moving scatterers. Owing to high path loss, we neglect the energy contribution of remote scatterers.

For ease of reference, the parameters introduced in this geometrical model are summarized in Table 1. It is assumed that T_X and R_X can move with nonlinearly varying velocities in nonlinearly varying directions according to different roadway scenarios (e.g., flat roads, intersections and arcuate overpasses). Each local scatterer can move with a random velocity in a random direction.

Table 1. Definition of the parameters used in the geometrical model.

Symbol	Definition
S	The local moving scatterer.
D	The distance between T_x and R_x.
q, p	The antenna element identifier of T_x and R_x, respectively.
Q, P	The number of antenna elements of T_x and R_x, respectively.
d_r, d_R	The spacing between two adjacent antenna elements of T_x and R_x, respectively.
α_q, β_q	The azimuth angle and elevation angle of T_x's antenna array, respectively.
α_p, β_p	The azimuth angle and elevation angle of R_x's antenna array, respectively.
$\alpha_{pq}^T, \beta_{pq}^T$	The azimuth angle and elevation angle of AoD, respectively.
$\alpha_{pq}^R, \beta_{pq}^R$	The azimuth angle and elevation angle of AoA, respectively.
v_T, v_R, v_S	The velocities of T_X, R_X and S, respectively.
α_T, β_T	The azimuth angle and elevation angle of v_T, respectively.
α_R, β_R	The azimuth angle and elevation angle of v_R, respectively.
$\alpha_{pq}^S, \beta_{pq}^S$	The azimuth angle and elevation angle of v_S, respectively.

2.2. Reference Model

As shown in Fig. 1, the impulse response $h_{pq}(t)$ of the channel $q \to p$ is a superposition of LoS and SB components and can be written as

$$h_{pq}(t) = h_{pq}^{LoS}(t) + h_{pq}^{SB}(t), \tag{1}$$

$$h_{pq}^{LoS}(t) = \rho_{pq} \exp\left\{ j \left[2\pi f_{pq,\rho} t + 2\pi \left(f_{pq,\rho}^{q} + f_{pq,\rho}^{p} \right) + \theta_{pq,\rho} \right] \right\}, \tag{2}$$

$$h_{pq}^{SB}(t) = \lim_{N \to \infty} \sum_{n=1}^{N} c_{pq,n} \exp\left\{ j \left[2\pi f_{pq,n} t + 2\pi \left(f_{pq,n}^{q} + f_{pq,n}^{p} \right) + \theta_{pq,n} \right] \right\}, \tag{3}$$

where ρ_{pq}, $c_{pq,n}$ are the path amplitudes; $f_{pq,\rho}$, $f_{pq,n}$ are the Doppler shifts; $\theta_{pq,\rho}$, $\theta_{pq,n}$ are the phase shifts; $f^q_{pq,\rho}$, $f^q_{pq,n}$ are the frequency shifts for qth antenna element of T_X; N is the path number of $h^{SB}_{pq}(t)$; $f^p_{pq,\rho}$, $f^p_{pq,n}$ are the frequency shifts for pth antenna element of R_X.

According to the central limit theorem, $h^{SB}_{pq}(t)$ equals a complex valued Gaussian random process with a zero mean and a variance $2\sigma^2 = Var\{h^{SB}_{pq}(t)\} = \lim\limits_{N\to\infty}\sum\limits_{n=1}^{N} E[c^2_{pq,n}]$. In this paper,the channel gain of $h_{pq}(t)$ is normalized, i.e., $2\sigma^2 + \rho^2_{pq} = 1$, so the Rice factor is $K = \rho^2_{pq}/2\sigma^2$. The phase shifts are introduced by the moving scatterers T_X and R_X. Without loss of generality, we can assume that the phases $\theta_{pq,\rho}$ and $\theta_{pq,n}$ are uniformly distributed on the interval $[0, 2\pi)$ and independent of each other.

The difference of the total propagation distance (TPD) between $h_{pq}(t)$ and $h_{11}(t)$ result from frequency shifts $f^q_{pq,\rho}, f^p_{pq,\rho}, f^q_{pq,n}$ and $f^p_{pq,n}$. The Doppler shifts $f_{pq,\rho}$ and $f_{pq,n}$ are caused by the movement of the transceiver and scatterers. The AoD and AoA of LoS rays can be approximately equal to zero due to $\max(d_T, d_R) \ll D$. According to the projection theory $f^q_{pq,\rho}, f^p_{pq,\rho}, f^q_{pq,n}, f^p_{pq,n}$ and $f_{pq,\rho}$ can be derived, respectively

$$f^a_{pq,\rho} = \frac{(a-1)\, d_b f_0}{c} \cos\alpha_a \cos\beta_a, \tag{4}$$

$$f^a_{pq,n} = \frac{(a-1)\, d_b f_0}{c} \left[\cos\left(\alpha_a - \alpha^b_{pq}\right)\cos\beta_a \cos\beta^b_{pq} + \sin\beta_a \sin\beta^b_{pq}\right], \tag{5}$$

$$f_{pq,\rho} = \frac{f_0}{c}\left(v_T \cos\alpha_T \cos\beta_T + v_R \cos\alpha_R \cos\beta_R\right), \tag{6}$$

$$\begin{aligned} f_{pq,n} \;=\; & f^T_{pq} + f^R_{pq} + f^{AOD}_{pq,n} + f^{AOA}_{pq,n} = \frac{f_0}{c}\left\{v_T\left[\cos\left(\alpha_T - \alpha^T_{pq}\right)\cos\beta_T \cos\beta^T_{pq} + \sin\beta_T \sin\beta^T_{pq}\right]\right. \\ & + v_R\left[\cos\left(\alpha_R - \alpha^R_{pq}\right)\cos\beta_R \cos\beta^R_{pq} + \sin\beta_R \sin\beta^R_{pq}\right] \\ & + v_S\left[\cos\left(\alpha^S_{pq} - \alpha^T_{pq}\right)\cos\beta^S_{pq} \cos\beta^T_{pq} + \sin\beta^S_{pq} \sin\beta^T_{pq}\right] \\ & \left. + v_S\left[\cos\left(\alpha^S_{pq} - \alpha^R_{pq}\right)\cos\beta^S_{pq} \cos\beta^R_{pq} + \sin\beta^S_{pq} \sin\beta^R_{pq}\right]\right\}, \end{aligned} \tag{7}$$

where $a = q, p$, and $b = T, R$, respectively; f_0 is the carrier frequency; c is the speed of the signal.

3. SPACE-TIME CORRELATION FUNCTION AND DOPPLER POWER SPECTRAL DENSITY

Based on the reference model, the ST-CF and D-PSD can be obtained for 3-D V2V MIMO multipath fading channels indifferent roadway scenarios.

3.1. Space-Time Correlation Function

According to the definition of ST-CF, the normalized ST-CF between $h_{pq}(t)$ and $h_{\bar{p}\bar{q}}(t)$ is

$$R_{\bar{p}\bar{q},pq}(d_T, d_R, \tau) = E\left[h_{\bar{p}\bar{q}}(t)^* h_{pq}(t+\tau)\right], \tag{8}$$

where $(\bullet)^*$ is the complex conjugate operation, $E(\cdot)$ the statistical expectation operator, and $\bar{p}$ and $\bar{q}$ are also the antenna element identifiers of R_X and T_X, respectively.

Since $h^{LoS}_{pq}(t)$ and $h^{SB}_{pq}(t)$ are independent of each other [10], the normalized ST-CF in Eq. (8) can be simplified as a superposition of the normalized ST-CFs $R^{SB}_{\bar{p}\bar{q},pq}(d_T, d_R, \tau)$ and $R^{LoS}_{\bar{p}\bar{q},pq}(d_T, d_R, \tau)$ of the SB and LoS components, i.e.,

$$R_{\bar{p}\bar{q},pq}(d_T, d_R, \tau) = R^{SB}_{\bar{p}\bar{q},pq}(d_T, d_R, \tau) + R^{LoS}_{\bar{p}\bar{q},pq}(d_T, d_R, \tau), \tag{9}$$

3.1.1. ST-CF of LoS Component

According to Eq. (2), the ST-CF of the LoS component can be written as

$$\begin{aligned} R^{LoS}_{\bar{p}\bar{q},pq}(d_T, d_R, \tau) = \rho_{pq}\rho_{\bar{p}\bar{q}} E\left\{\exp\left\{j\left[2\pi t\left(f_{pq,\rho} - f_{\bar{p}\bar{q},\rho}\right) + 2\pi f_{pq,\rho}\tau\right.\right.\right. \\ \left.\left.\left. + 2\pi\left(f^q_{pq,\rho} + f^p_{pq,\rho} - f^{\bar{q}}_{\bar{p}\bar{q},\rho} - f^{\bar{p}}_{\bar{p}\bar{q},\rho}\right) + \theta_{pq,\rho} - \theta_{\bar{p}\bar{q},\rho}\right]\right\}\right\}. \end{aligned}$$

$E\{\exp[j(\theta_{pq,\rho}-\theta_{\bar{p}\bar{q},\rho})]\}$ equals 1 under the assumption that $\theta_{pq,\rho}$ and $\theta_{\bar{p}\bar{q},\rho}$ are uniformly distributed and independent of each other. We assume ρ_{pq} equals $\rho_{\bar{p}\bar{q}}$ due to $\max(d_T, d_R) \ll D$. Then, Eq. (10) can be written as

$$R^{LoS}_{\bar{p}\bar{q},pq}(d_T, d_R, \tau) = \rho^2_{pq} E\left\{\exp\left[j2\pi\left(f_{pq,\rho}\tau + \Delta f_\rho\right)\right]\right\} = \rho^2_{pq}\exp\left[j2\pi\left(f_{pq,\rho}\tau + \Delta f_\rho\right)\right], \tag{10}$$

$$\Delta f_\rho = f^q_{pq,\rho} + f^p_{pq,\rho} - f^{\bar{q}}_{\bar{p}\bar{q},\rho} - f^{\bar{p}}_{\bar{p}\bar{q},\rho} = \frac{f_0}{c}\left[(q-\bar{q})\, d_T \cos\alpha_q \cos\beta_q + (p-\bar{p})\, d_R \cos\alpha_p \cos\beta_p\right]. \tag{11}$$

3.1.2. ST-CF of SB Component

According to Eq. (3), the ST-CF of the SB component can be written as

$$\begin{aligned} R^{SB}_{\bar{p}\bar{q},pq}(d_T, d_R, \tau) = \lim_{N\to\infty}\lim_{N\to\infty}\sum_{n=1}^{N} c_{\bar{p}\bar{q},n}\sum_{n=1}^{N} c_{pq,n} E\left\{\exp\left\{j\left[2\pi\left(f_{pq,n} - f_{\bar{p}\bar{q},n}\right)t + 2\pi f_{pq,n}\tau\right.\right.\right. \\ \left.\left.\left. + 2\pi\left(f^q_{pq,n} + f^p_{pq,n} - f^{\bar{q}}_{\bar{p}\bar{q},n} - f^{\bar{p}}_{\bar{p}\bar{q},n}\right) + \theta_{pq,n} - \theta_{\bar{p}\bar{q},n}\right]\right\}\right\}. \end{aligned} \tag{12}$$

It is assumed that $c_{\bar{p}\bar{q},n} = c_{pq,n} = \sigma\sqrt{2/N}$, i.e., all the path amplitudes in Eq. (3) have the same size. Then,

$$R^{SB}_{\bar{p}\bar{q},pq}(d_T, d_R, \tau) = 2\sigma^2 \lim_{N\to\infty}\sum_{n=1}^{N} E\left\{\exp\left[j2\pi\left(f_{pq,n}\tau + \Delta f_n\right)\right]\right\}, \tag{13}$$

$$\begin{aligned} \Delta f_n = f^q_{pq,n} + f^p_{pq,n} - f^{\bar{q}}_{\bar{p}\bar{q},n} - f^{\bar{p}}_{\bar{p}\bar{q},n} = \frac{f_0}{c}\left\{(q-\bar{q})\, d_T\left[\cos\left(\alpha_q - \alpha^T_{pq}\right)\cos\beta_q\cos\beta^T_{pq}\right.\right. \\ \left.\left. + \sin\beta_q\sin\beta^T_{pq}\right] + (p-\bar{p})\, d_R\left[\cos\left(\alpha_p - \alpha^R_{pq}\right)\cos\beta_p\cos\beta^R_{pq} + \sin\beta_p\sin\beta^R_{pq}\right]\right\}. \end{aligned} \tag{14}$$

Since number N of local scatterers is approximately infinite, the angles $\alpha^T_{pq}, \alpha^R_{pq}, \alpha^S_{pq}, \beta^T_{pq}, \beta^R_{pq}$ and β^S_{pq} become continuous random variables with probability density functions (PDFs) $p(\bullet)$. Then, the ST-CF in Eq. (13) can be written as

$$\begin{aligned} R^{SB}_{\bar{p}\bar{q},pq}(d_T, d_R, \tau) = 2\sigma^2 \int\int\int\int\int\int\int \exp\left[j2\pi\left(f_{pq,n}\tau + \Delta f_n\right)\right] p\left(\nu^S_{pq}\right) p\left(\alpha^S_{pq}, \beta^S_{pq}\right) \\ \times p\left(\alpha^T_{pq}, \beta^T_{pq}, \alpha^R_{pq}, \beta^R_{pq}\right) d\nu^S_{pq} d\alpha^S_{pq} d\beta^S_{pq} d\alpha^T_{pq} d\beta^T_{pq} d\alpha^R_{pq} d\beta^R_{pq}. \end{aligned} \tag{15}$$

Due to the complex nature of joint distribution of AoD and AoA $p(\alpha^T_{pq}, \beta^T_{pq}, \alpha^R_{pq}, \beta^R_{pq})$, it is assumed that the angles are independent of each other [6, 7]. The ST-CF in Eq. (15) is a generalized and parametric expression, and its parameters such as the random angles, velocities of the moving scatterers, the velocity and direction of transceiver can be calculated as follows.

- Angle distributions. We use the uniform distributions to characterize the random angles $\alpha^T_{pq}, \alpha^R_{pq}, \alpha^S_{pq}, \beta^T_{pq}, \beta^R_{pq}$ and β^S_{pq}. The interval of azimuth angles is $(-\pi, \pi]$, and the interval of elevation angles is $(-\pi/2, \pi/2]$.
- Scatterer velocity distributions. In this regard, we use the uniform distribution to describe the velocity moving scatterers.
- Transceiver velocity and direction. The velocity and direction of transceiver change over time according to different roadway scenarios as shown in Fig. 2: i. flat roads; ii. intersections; iii. arcuate overpasses. They can be modeled as

$$v_{T/R}(t_{i+1}) = a_{T/R}(t_{i+1} - t_i) + v_{T/R}(t_i), \tag{16}$$

$$\alpha_{T/R}(t_{i+1}) = \begin{cases} b_{T/R}(t_{i+1} - t_i) + \alpha_{T/R}(t_i), & \text{for i. and iii.,} \\ -\dfrac{v_{T/R}(t_i)}{r_1}(t_{i+1} - t_i) + \alpha_{T/R}(t_i), & \text{for ii.,} \end{cases} \tag{17}$$

$$\beta_{T/R}(t_{i+1}) = \begin{cases} -\dfrac{v_{T/R}(t_i)}{r_2}(t_{i+1} - t_i) + \beta_{T/R}(t_i), & \text{for iii.,} \\ 0 & \text{for i. and ii.,} \end{cases} \tag{18}$$

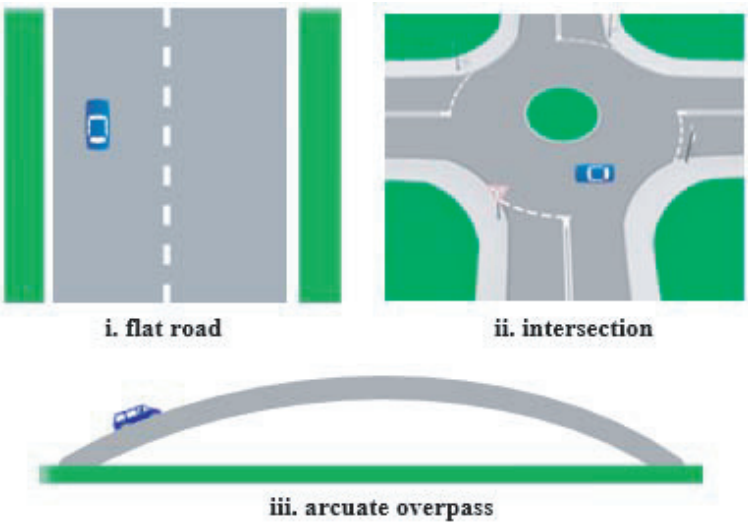

Figure 2. Roadway scenarios.

where $v_{T/R}(t_i), \alpha_{T/R}(t_i), \beta_{T/R}(t_i)$ are the initial values of the velocity and direction of transceiver at $t = t_i$; $a_{T/R}, b_{T/R}$ are the rates of changes; r_1 is the turning radius of the intersections; r_2 is the radius of the arcuate overpass. Because the velocity and direction of transceiver change nonlinearly in the actual V2V communications, $a_{T/R}$ and $b_{T/R}$ are not constant and change randomly in certain intervals over time.

3.2. Doppler Power Spectral Density

The D-PSD can be obtained by taking the Fourier transform of the ST-CF in Eq. (9) with respect to time difference, i.e.,

$$S_{\bar{p}\bar{q},pq}(d_T, d_R, \omega) = \mathcal{F}_\tau \{R_{\bar{p}\bar{q},pq}(d_T, d_R, \tau)\} = S^{SB}_{\bar{p}\bar{q},pq}(d_T, d_R, \omega) + S^{LoS}_{\bar{p}\bar{q},pq}(d_T, d_R, \omega). \tag{19}$$

According to Eq. (10), the D-PSD of the LoS component can be written as

$$S^{LoS}_{\bar{p}\bar{q},pq}(d_T, d_R, \omega) = 2\pi\rho^2_{pq} \exp(j2\pi f_\rho)\, \delta(\omega - 2\pi f_{pq,\rho}), \tag{20}$$

where $\delta(\bullet)$ is the Dirac delta function.

The closed-form expression of D-PSD cannot be obtained due to the multiple integral of the ST-CF of the SB component. In Section 4, the D-PSD is shown by means of numerical simulations

4. RESULTS AND VALIDATION

This section demonstrates the normalized ST-CFs and validates the D-PSD described in Section 3 through the numerical simulation. Unless indicated otherwise, the values of the simulation parameters are summarized in Table 2.

4.1. ST-CFs in Different Roadway Scenarios

4.1.1. ST-CFs in Flat Road Scenarios

Figure 3 demonstrates the absolute ST-CFs in Eq. (9) for the 3-D fixed scattering and moving scattering in flat road scenarios. The transmitter and receiver move with constant velocities in constant directions. The scatterer velocity is zero and uniformly distributed for the fixed scattering and moving scattering, respectively. The other parameters used to obtain curves in Fig. 3 are summarized in Table 2. As shown in Fig. 3, the ST-CFs decrease faster for moving scattering than fixed scattering, and the larger

Table 2. Parameters used in the numerical simulation.

Parameters	Fig. 3	Fig. 4	Fig. 5	Fig. 6	Fig. 7	Parameters	Fig. 3	Fig. 4	Fig. 5	Fig. 6	Fig. 7
f_0 (GHz)	5.9	5.9	5.9	5.9	2.435	$v_T(0)$ (m/s)	20	20	20	20	12
K	2	2	2	2	2.41	$v_R(0)$ (m/s)	23	23	23	23	12
q, p	2, 2	2, 2	2, 2	2, 2	1, 1	$\overline{v_S}$ (m/s)	0, 10, 15	15	15	15	4.5
$\bar{q}$, $\bar{p}$	1, 1	1, 1	1, 1	1, 1	1, 1	$\alpha_T(0)$ (rad)	$\pi/2$	$\pi/2$	$\pi/2$	$\pi/2$	$\pi/2$
d_T, $d_R(\lambda)$	1/2, 1/2	1/2, 1/2	1/2, 1/2	1/2, 1/2	0, 0	$\alpha_R(0)$ (rad)	$\pi/2$	$\pi/2$	$\pi/2$	$\pi/2$	$\pi/2$
α_q, β_q (rad)	$\pi/2, \pi/6$	$\pi/2, \pi/6$	$\pi/2, \pi/6$	$\pi/2, \pi/6$	0, 0	$\beta_T(0)$ (rad)	0	0	0	$\pi/4$	0
α_p, β_p (rad)	$\pi/2, \pi/6$	$\pi/2, \pi/6$	$\pi/2, \pi/6$	$\pi/2, \pi/6$	0, 0	$\beta_R(0)$ (rad)	0	0	0	$0, \pi/4$	0

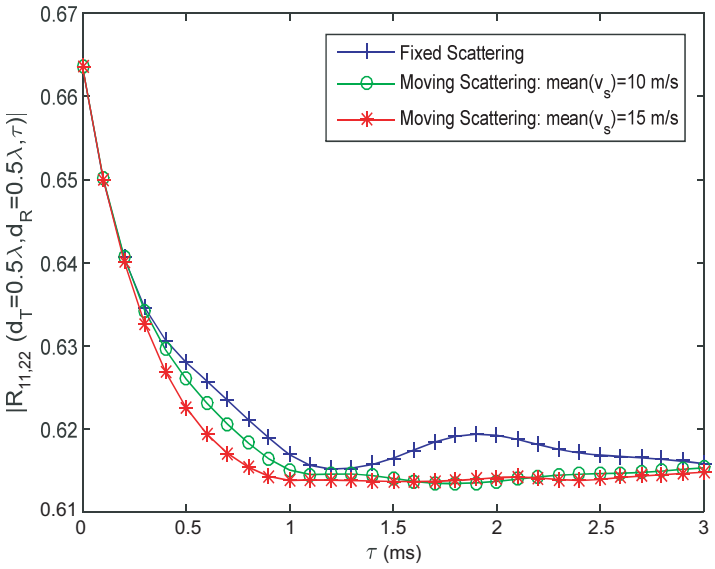

Figure 3. Absolute ST-CFs for 3-D fixed and moving scattering scenarios.

the mean scatterer velocity $\overline{v_S}$ is, the faster ST-CFs decrease. The comparison results indicate the large-scale antenna arrays with the same spacing between two adjacent antenna elements have lower correlation for 3-D moving scattering. Moving foliage, walking pedestrians and passing vehicles are the main scatterers in motion in real-world V2V communication environments, and their effect on the channel characteristics cannot be ignored.

Figure 4 demonstrates the absolute ST-CFs in Eq. (9) for the 3-D moving scattering at the time $t = 3$ and 6 s in flat road scenarios. The transmitter and receiver move with varying velocities in constant horizontal directions for ST-CFs demonstrated by red curves, and move with varying velocities in varying horizontal directions for ST-CFs demonstrated by black curves. Because the velocity and horizontal direction of transceiver motion change nonlinearly in the actual V2V communications,the rates of changes $a_{T/R}, b_{T/R}$ are obtained randomly from intervals $[-2, 2]$ and $[-\pi/7, \pi/7]$ respectively. The other parameters used to obtain curves in Fig. 4 are summarized in Table 2. As shown in Fig. 4, both varying velocities and varying horizontal directions of the transceiver motion have effect on the ST-CFs of the 3-D V2V moving scattering channel in flat road scenarios. Furthermore, the effect of varying horizontal directions is relatively more significant. Figs. 3 and 4 show that the research on the model and statistical properties of moving scattering and transceiver motion is necessary.

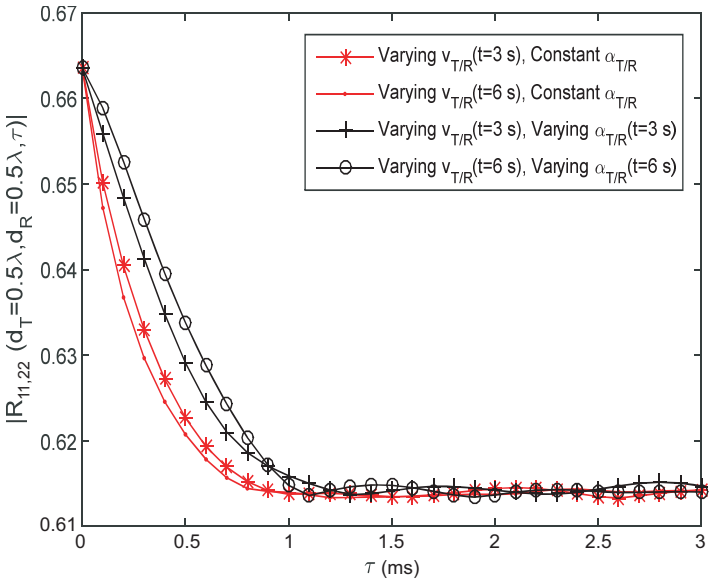

Figure 4. Absolute ST-CFs at different time for 3-D moving scattering.

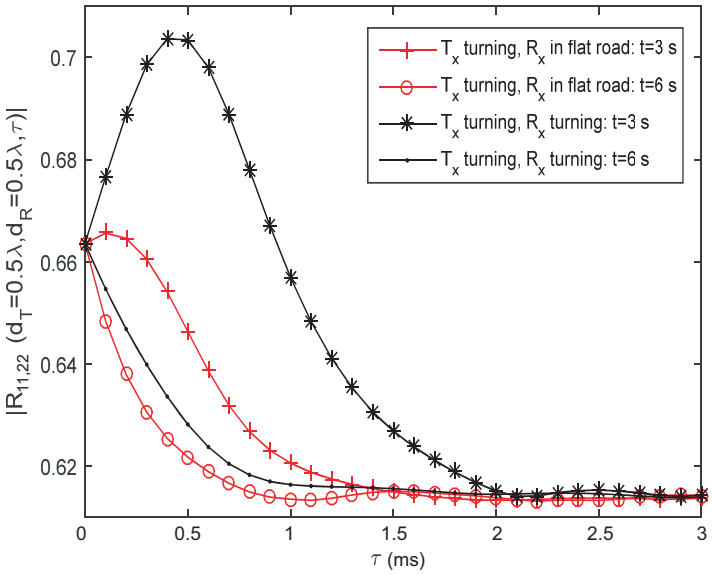

Figure 5. Absolute ST-CFs at different time in intersection scenarios.

4.1.2. ST-CFs in Intersection Scenarios

Figure 5 demonstrates the absolute ST-CFs in Eq. (9) for the 3-D moving scattering at the time $t = 3$ and 6 s in intersection scenarios. The transmitter and receiver also move with varying velocities in varying horizontal directions. The rates of changes $a_{T/R}$ are obtained randomly from the interval $[-2, 2]$, and b_R for ST-CFs demonstrated by red curves are obtained randomly from the interval $[\pi/7, \pi/7]$. The turning radius r_1 of the transceiver is 8 m. The other parameters used to obtain curves in Fig. 5 are summarized in Table 2. As shown in Fig. 5, varying horizontal directions determined by transceiver velocities and the turning radius have significant effect on the ST-CFs of the 3-D V2V moving scattering channel in intersection scenarios. Different from Fig. 4, ST-CF curves at $t = 3$ s in Fig. 5 have upward oscillations resulting in the curves converge to the bottoms lowly, and this may be caused by varying horizontal directions of the transceiver which is turning in the intersection.

4.1.3. ST-CFs in Arcuate Overpass Scenarios

Figure 6 demonstrates the absolute ST-CFs in Eq. (9) for the 3-D moving scattering at the time $t = 3$ and 6 s in arcuate overpass scenarios. The transmitter and receiver move with varying velocities in varying 3-D directions. The rates of changes $a_{T/R}, b_{T/R}$ are obtained randomly from intervals $[-2, 2]$ and $[\pi/7, \pi/7]$, respectively. The radius r_2 of the arcuate overpass is 15 m. The other parameters used to obtain curves in Fig. 6 are summarized in Table 2. As shown in Fig. 6 varying vertical directions determined by transceiver velocities and the arcuate overpass radius have significant effect on the ST-CFs of the 3-D V2V moving scattering channel in arcuate overpass scenarios. Similar to Fig. 5, black curves in Fig. 6 also have upward oscillations which may be caused by varying vertical directions of the transceiver motion. According to Figs. 4–6, it is very necessary and valuable for future V2V communications that 3-D directions of the transceiver's antennas or beamforming can be adjusted in real time to reduce the harmful effect of the transceiver's motion in varying directions.

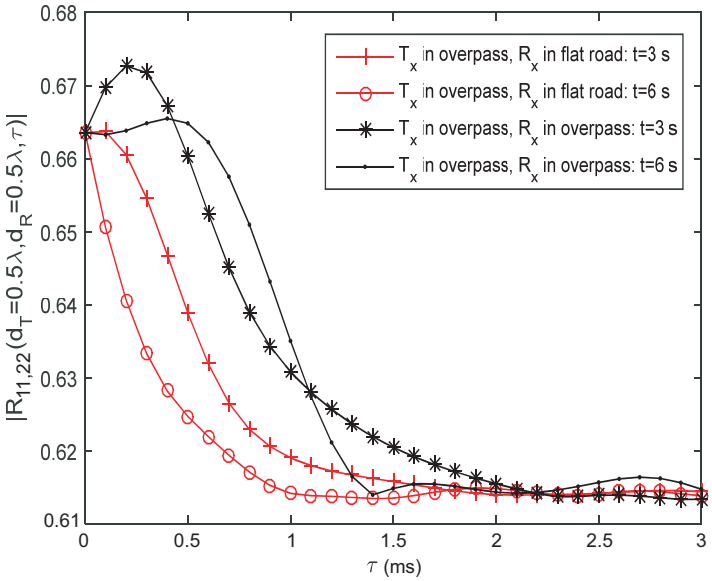

Figure 6. Absolute ST-CFs at different time in arcuate overpass scenarios

4.2. Comparison with Measurements

D-PSD is one of the most important and unique channel characteristics for V2V communication channels. To illustrate the validity of the proposed model, we compare the modeled D-PSDs of the 3-D V2V moving scattering channel in flat road scenarios with the theoretical V2V D-PSDs described in [10] and [17] and the measured V2V D-PSD described in [19].

Figure 7 demonstrates the comparison among the modeled D-PSD obtained from the Fourier transform of the ST-CF presented in Eq. (9) at $t = 6$ s, the theoretical D-PSD of Fig. 8 in [10], the theoretical D-PSD of Fig. 11 in [17], and the measured D-PSD of Fig. 11 in [19]. The theoretical D-PSD in [10] reproduced here is based on the two-cylinder model with moving and stationary scatterers for $d_R = d_T = 0$. The theoretical D-PSD in [17] reproduced here is based on the generic MIMO V2V fading channel model with multiple moving scatterers for $d_R = d_T = 0$. The channel measurements in [19] for the measured D-PSD were collected at 2.435 GHz in the urban street surface environment, and the spacing between two adjacent antenna elements of T_X and R_X was set to zero. In the simulation the transmitter and receiver also move with varying velocities in varying horizontal directions. The rates of changes $a_{T/R}, b_{T/R}$ are also obtained randomly from intervals $[-2, 2]$ and $[\pi/7, \pi/7]$, respectively. The other parameters used to obtain the modeled D-PSD curve in Fig. 7 are summarized in Table 2. Fig. 8 demonstrates the cumulative distribution functions (CDFs) of the relative deviations between modeled/theoretical D-PSDs and measured values in Fig. 7. The mean relative deviation of the modeled

D-PSDs and theoretical D-PSDs in [17] and [10] are 2.75%, 3.9% and 8.32%, respectively. As shown in Fig. 8, about 90% of the relative deviations of modeled D-PSDs in Fig. 7 are less than 5%, and the relative deviations of theoretical D-PSDs are explicitly larger than those of modeled D-PSDs. According to Figs. 7 and 8, the modeled D-PSD matches better with measured D-PSD than the theoretical D-PSDs in [17] and [10]. The acceptable matches in Figs. 7 and 8 confirm the utility of the proposed model and show the need for including varying velocities and directions of the transceiver motion in propagation model.

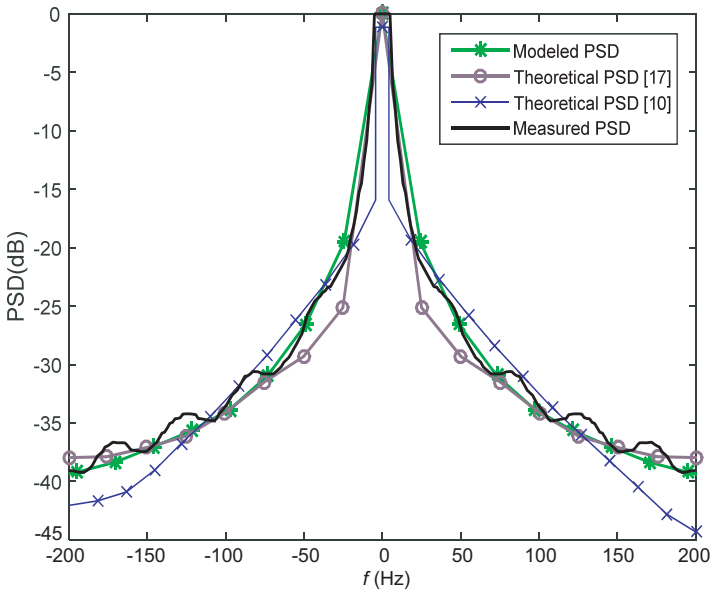

Figure 7. Comparison among the modeled D-PSD, the theoretical D-PSDs in [10] and [17], and the measured D-PSD in [19].

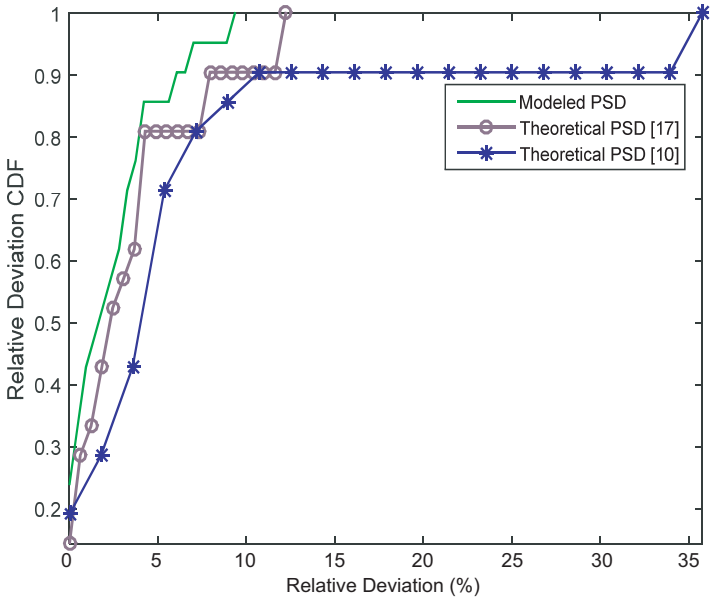

Figure 8. The relative deviation CDFs of modeled and theoretical PSDs in Fig. 7.

5. CONCLUSION

Taking account of nonlinearly varying velocities and directions of the transceiver motion indifferent roadway scenarios (e.g., flat roads, intersections and arcuate overpasses), a 3-D geometrical moving scattering propagation model that includes LoS and SB links between the transmitter and receiver was proposed. Then, a 3-D reference model for narrowband MIMO V2V multipath fading channels was developed. Based on the reference model, the corresponding expressions and numerical results of ST-CFs and D-PSDs were studied for different roadway scenarios. It has been shown that the moving scattering, nonlinearly varying velocities and directions of the transceiver motion have significant effect on the ST-CFs. Finally, the modeled D-PSD in flat road scenarios were compared with the measured data and other literature's theoretical results. The close agreements between the analytically and empirically obtained D-PSDs confirmed the utility of the proposed model and showed the importance of including moving scatterers, nonlinearly varying velocities and directions of the transceiver motion in the propagation model.

ACKNOWLEDGMENT

This work was funded by the National Natural Science Foundation of China (No. 91438104, No. 61501065 and No. 61571069), the Fundamental Research Funds for the Central Universities (No. 106112016CDJXY160001 and No. 106112017CDJQJ168817) and the Chongqing Research Program of Basic Research and Frontier Technology (No. CSTC2016JCYJA0021).

REFERENCES

1. Walter, M., D. Shutin, and U.-C. Fiebig, "Delay-dependent doppler probability density functions for vehicle-to-vehicle scatter channels," *IEEE Trans. Antennas and Propag.*, Vol. 62, No. 4, 2238–2249, Apr. 2014.
2. Yuan, Y., C. X. Wang, X. Cheng, B. Ai, and D. I. Laurenson, "Novel 3D geometry-based stochastic models for non-isotropic MIMO vehicle-to-vehicle channels," *IEEE Trans. Wireless Commun.*, Vol. 13, No. 1, 298–309, Jan. 2014.
3. Ndzi, D. L., K. Stuart, S. Toautachone, B. Vuksanovic, and D. A. Sanders, "Wideband sounder for dynamic and static wireless channel characterisation: Urban picocell channel model," *Progress In Electromagnetics Research*, Vol. 113, 285–312, 2011.
4. Chelli, A. and M. Pätzold, "The impact of fixed and moving scatterers on the statistics of MIMO vehicle-to-vehicle channels," *Proc. IEEE VTC Spring*, 1–6, Barcelona, Spain, Apr. 2009.
5. Chelli, A. and M. Pätzold, "A dynamic MIMO vehicle-to-vehicle channel model derived from the geometrical street model," *Proc. IEEE VTC Fall*, 1–6, San Francisco, CA, USA, Sep. 2011.
6. Borhani, A. and M. Pätzold, "Modeling of vehicle-to-vehicle channels in the presence of moving scatterers," *Proc. 76th IEEE VTC-Fall*, 1–5, Quebec City, QC, Canada, Sep. 2012.
7. Borhani, A. and M. Pätzold, "Correlation and spectral properties of vehicle-to-vehicle channels in the presence of moving scatterers," *IEEE Trans. Veh. Technol.*, Vol. 62, No. 9, 4228–4239, Nov. 2013.
8. Soltani, M. D., M. Alimadadi, Y. Seyedi, and H. Amindavar, "Modeling of Doppler spectrum in V2V urban canyon oncoming environment," *Proc. IEEE Int. Workshop IST*, 1155–1160, Tehran, Iran, Sep. 2014.
9. Soltani, M. D., M. Alimadadi, and A. Mohammadi, "Modeling of mobile scatterer clusters for Doppler spectrum in wideband vehicle-to-vehicle communication channels," *IEEE Commun. Lett.*, Vol. 18, No. 4, 628–631, Apr. 2014.
10. Zajić, A. G., "Impact of moving scatterers on vehicle-to-vehicle narrow-band channel characteristics," *IEEE Trans. Veh. Technol.*, Vol. 63, No. 7, 3094–3106, Sep. 2014.
11. Zajić, A. G., "Modeling impact of moving scatterers on Doppler spectrum in wideband vehicle-to-vehicle channels," *Proc. Eur. Conf. Antennas Propag.*, 1–5, Lisbon, May 2015.

12. Liang, X., X. Zhao, S. Li, Q. Wang, and J. Li, "A dynamic geometry-based scattering model for street vehicle-to-vehicle wideband MIMO channels," *Proc. IEEE 26th Annual International PIMRC*, 2239–2243, Hong Kong, Sep. 2015.
13. Zhao, X., X. Liang, S. Li, and B. Ai, "Two-cylinder and multi-ring GBSSM for realizing and modeling of vehicle-to-vehicle wideband MIMO channels," *IEEE Trans. Intell. Trans. Syst.*, Vol. 17, No. 10, 2787–2799, Oct. 2016.
14. Fuhl, J., J.-P. Rossi, and E. Bonek, "High-resolution 3-D direction-ofarrival determination for urban mobile radio," *IEEE Trans. Antennas Propag.*, Vol. 45, No. 4, 672–682, Apr. 1997.
15. Kalliola, K., K. Sulonen, H. Laitinen, O. Kivelas, J. Krogerus, and P. Vainikainen, "Angular power distribution and mean effective gain of mobile antenna in different propagation environments," *IEEE Trans. Veh. Technol.*, Vol. 51, No. 5, 823–838, Dec. 2002.
16. Karadimas, P. and D. Matolak, "Generic stochastic modeling of vehicle-to-vehicle wireless channels," *Vehicular Communications*, Vol. 1, No. 4, 153–167, Aug. 2014.
17. Du, D., X. Zeng, X. Jian, L. Miao, and H. Wang, "Three-dimensional vehicle-to-vehicle channel modeling with multiple moving scatterers," *Mobile Information Systems*, Vol. 2017, 1–14, Jul. 2017.
18. Dahech, W., M. Pätzold, and N. Youssef, "A dynamic mobile-to-mobile multipath fading channel model taking account of velocity variations of the mobile stations," *Proc. IEEE EuCAP*, 1–4, Lisbon, Apr. 2015.
19. Zajić, A. G., G. Stüber, T. Pratt, and S. Nguyen, "Wideband MIMO mobile-to-mobile channels: Geometry-based statistical modeling with experimental verification," *IEEE Trans. Veh. Technol.*, Vol. 58, No. 2, 517–534, Feb. 2009.